

# Micro-arcsecond Line-of-Sight Filtered Performance for Spacecraft Formation Flying

William D. Banas\* and John L. Crassidis†

*University at Buffalo, State University of New York, Amherst, NY 14260-4400*

Formation Flying is the concept that multiple spacecraft can be arranged in a formation to perform tasks that are not possible with a single spacecraft, or tasks that can be done more efficiently or inexpensively with a group of small spacecraft. One of the main engineering problems to be overcome is that of orienting or pointing a spacecraft to a very high degree of precision. Many approaches have focused on improving the performance and accuracy of the hardware used to determine the current orientation of the spacecraft. Here, orientation is related to the line-of-sight accuracy between one spacecraft and another, not the overall relative attitude. The approach in this paper explores filtering algorithms for the goal of determining the minimum hardware requirements necessary to obtain micro-arcsecond line-of-sight pointing knowledge. This may allow for the use of less expensive hardware in future formation flying missions and may vastly improve mission capability.

## I. Introduction

Spacecraft formation flying, also known as distributed space systems (DSS), has become an increasingly important area of research. The development of formation flying technology is necessary if NASA is to be successful in implementing President Bush's 2004 vision for the United States civil space program. In the report detailing this vision, formation flying was identified as one of seventeen "enabling technologies" which are "critical to attainment of exploration objectives within reasonable schedules and affordable costs" and, by extension, "will significantly help the United States to protect its technological leadership, economic vitality, and security."<sup>1</sup>

Significant performance, robustness, maintenance and cost benefits of a formation made up of smaller, individual spacecraft can be realized for a variety of military, civilian and scientific applications. Collection of information through a cluster of individual sensors or through sensors distributed over multiple formation flying vehicles can provide substantial benefits.<sup>2</sup> The advantages of a constellation of small spacecraft are many. Smaller and lighter spacecraft are much less expensive to launch. Spare spacecraft can be flown in formation and repositioned into place if a spacecraft fails, thus saving on mission downtime and the prospect of an expensive repair mission (if repair is indeed possible at all). DSS will enable higher resolution imagery, robust and redundant fault-tolerant spacecraft system architectures, and complex networks dispersed over clusters of spacecraft.<sup>3</sup>

For example, instead of the deployment of a single large spacecraft, such as the Hubble Space Telescope, a cluster of smaller spacecraft can be deployed to effectively create a much larger, higher resolution telescope through the concept of interferometry; a concept commonly used to link together ground-based radio telescopes across the surface of the Earth. Spare or backup spacecraft can be deployed in formation. Spacecraft launches and replacement can be conducted unmanned. Thus, mission cost can be decreased while mission capability, robustness and lifecycle can all be increased. The prospect of scuttling an entire large spacecraft and, indeed, the cancelation of the program itself, can be avoided. In the end, a multi-spacecraft design saves money and reduces risk. It is less expensive to build, launch and deploy smaller identical spacecraft. Also, with separate launches for individual spacecraft or perhaps for multiple spacecraft, if the design permits, one can avoid "putting all the eggs in one rocket."<sup>4</sup>

---

\*Graduate Student, Department of Mechanical and Aerospace Engineering, wdbanas@eng.buffalo.edu, Student Member AIAA.

†Associate Professor, Department of Mechanical and Aerospace Engineering, johnc@eng.buffalo.edu, Associate Fellow AIAA.

The difficulty with the concept of spacecraft formation flying or DSS is in determining the absolute and/or relative bearing of each spacecraft in the formation to a high degree of precision, particularly with respect to telescope and interferometry applications. To solve this problem, most approaches have focused on improvements in hardware through the development of a “super star tracker” or improved inertial references (e.g. low drift, low friction gyroscopes) to achieve alignments on the order of 30 micro-arcseconds.<sup>5</sup> Unfortunately, these hardware improvements may not be possible without disproportionate expenditures of time and money. This paper presents filtering approaches to achieve micro-arcsecond pointing knowledge through software. Here we focus on providing the minimum hardware requirements, in terms of required line-of-sight (LOS) measurement accuracy and required sampling rates. Micro-arcsecond pointing knowledge should be more than sufficient for all but the most ambitious DSS missions planned for the next 15-20 years.<sup>5,6</sup>

The organization of this paper is as follows. First, some of the current and proposed programs and missions are discussed, followed by a summary of the problems in achieving high accuracy knowledge. Then, the coordinate frames used in formation flying are shown, as well as the classical equations of motion. Next, the measurement model is discussed, followed by a simplification of this model to allow for linear models. These linear models will be used to determine the steady-state performance of a Kalman filtering using line-of-sight measurements. A simple analysis is also derived that relates filtered accuracy to sensor accuracy and sampling interval. Then, a summary of the nonlinear filters used for the full model is shown. Finally, simulation results are provided.

## A. Programs & Missions

As DSS technologies have matured in recent years, various groups and agencies are flying and proposing a large number of DSS missions.<sup>2,6</sup> Most of the significant scientific missions requiring DSS technology are incorporated under three NASA programs: New Millennium, Origins, and Structure and Evolution of the Universe (“Beyond Einstein”).

Near future DSS technology dependent missions associated with these programs include the Space Interferometry Mission (SIM) and the Laser Interferometer Space Antenna (LISA). Later missions such as the Terrestrial Planet Finder (TPF), the Planet Imager (PI) and Constellation-X, will depend upon the technologies developed for SIM and LISA. The New Millennium Space Technology 3 (ST3) mission, originally planned to launch in 2005, has since been cancelled. ST3 was to consist of two separate spacecraft to be used to test the techniques of interferometry and formation flying in space. ST3 would have been the first spaceborne stellar interferometer.<sup>5,7</sup>

The most ambitious with regard to DSS technology is the Micro-Arcsecond X-ray Imaging Mission (MAXIM), which will achieve resolution on the order of 100 nano-arcseconds to resolve the event horizon of a black hole. The MAXIM Pathfinder (MP) mission will lay the foundation for MAXIM with an angular resolution of roughly 100 micro-arcseconds. The Stellar Imager (SI) mission is another proposed 100 micro-arcsecond imaging mission.<sup>5,8,9</sup>

Each of these missions will need a stable relative reference accurate to a fraction of their angular resolution to produce quality images and data.<sup>5</sup> The goal of this research will be to do just that: to provide micro-arcsecond relative pointing knowledge, which will satisfy all but the most stringent requirements of any of these missions.

## B. Problem

Up to now, most approaches to achieving high precision angular resolution have concentrated on improvements in hardware. Typically, guidance systems for spacecraft have utilized (1) a star tracker to make use of guide stars, (2) an inertial reference, such a gyroscope, or (3) both. The simplest improvement to a star tracker would be to just make it bigger. Obviously, this increases the size and weight and still does not solve fundamental optics problems and limitations of CCDs. Use of the X-ray band (instead of the visible spectrum) will lead to problems because of the scarcity and “dimness” of targets, which means that it may not be scalable to the sub micro-arcsecond range required for MAXIM. Use of interferometry approaches like the SIM mission have been discounted due to high cost (nearly \$1 billion), which is much too expensive for a subsystem on another mission.<sup>5</sup> The main disadvantage of star trackers for formation flying applications is they provide absolute knowledge, which is useful for the primary spacecraft, but may not necessarily be the best choice for relative knowledge between spacecraft, i.e. using two inertial sensors to derive relative knowledge may be excessive.

Improvements to gyroscopes may be even more difficult to achieve. The Kilometric Optical Gyroscope (KOG) was dropped from the ST3 mission due to technical difficulties and cost. In theory, atomic interferometer gyroscope and the superfluid gyroscope have potential but will require much more development to produce a practical device. The Gravity Probe B (GP-B) gyroscopes utilize superconductivity (via cryogenics) to minimize drag and have been developed to near-flight readiness. They could be combined with a telescope and star tracker to achieve resolutions on the order of 100 micro-arcseconds to satisfy the requirements of the MP or SI missions.<sup>5</sup> However, they are still costly and their best resolution is far from satisfying the MAXIM requirements. In the final analysis, because star trackers and gyroscopes have been in use for a long time, they have reached a very high state of refinement, and are approaching their respective physical limitations. While it is tempting to attack the hardware problem head-on, we have reached a point of diminishing returns where it will take a great amount of money and effort to produce a comparatively small improvement in performance. In other words, star trackers and gyros are about as good as they are going to get, and any significant improvements may be a long way off.

## II. Approach

This work provides an assessment of the hardware requirements for future formation flying missions that have a goal of achieving accurate line-of-sight (LOS) information between two spacecraft (called a “chief” and a “deputy”). The LOS equipment may include microwave or laser technology. A promising technology involves a vision-based navigation (VISNAV) system, which comprises an optical sensor of a new kind combined with specific light sources (beacons) in order to achieve a selective or “intelligent” vision. The sensor is made up of a position sensing diode placed in the focal plane of a wide angle lens. Benefits of this configuration include: 1) very small sensor size, 2) very wide sensor field-of-view, 3) no complex/time consuming charge-coupling-device signal processing or pattern recognition required, 4) excellent rejection of ambient light interference under a wide variety of operating conditions, and 5) relatively simple electronic circuits with modest digital signal processing micro-computer requirements. A more detailed description of the VISNAV system can be found in Ref. 10.

Relative position and attitude results using a Kalman filter for spacecraft formation flying is shown in Ref. 11. However, the study only involved the feasibility of using LOS measurement for formation flying, and an analysis is not shown for obtaining the achievable accuracies in terms of sampling intervals and sensor accuracy. The LOS measurements and detailed relative orbital model equations will be combined in a Kalman filter to achieve micro-arcsecond directional knowledge in this current paper. To be clear, it is assumed that the chief spacecraft has perfect position and pointing knowledge and control with respect to some inertial frame (note that attitude is not considered). This paper does not address how this might be done, as this is a very difficult problem. The lone measurement is the relative LOS vector between the spacecraft. It is well known that using filtering algorithms provide more accuracy than sensors alone.<sup>12</sup> This paper only seeks to determine what hardware requirements might be necessary to achieve the goal of micro-arcsecond relative position and pointing knowledge between the deputy and chief spacecraft using filtering approaches. To be more realistic, it should be assumed that there is some relative motion of the deputy spacecraft with respect to the chief. To simulate this, a few micro-g’s of process noise are included in the analyses.

Here, an overview of the frames used to describe the relative attitude and position equations of motion is shown, reprinted for convenience from Ref. 11. The spacecraft about which all other spacecraft are orbiting is referred to as the chief. The remaining spacecraft are referred to as the deputies. The relative orbit position vector,  $\boldsymbol{\rho}$ , is expressed in components by  $\boldsymbol{\rho} = [x \ y \ z]^T$ , shown in Figure 1. The vector triad  $\{\hat{\mathbf{o}}_r, \hat{\mathbf{o}}_\theta, \hat{\mathbf{o}}_h\}$  is known as the Hill coordinate frame, where  $\hat{\mathbf{o}}_r$  is in the orbit radius direction,  $\hat{\mathbf{o}}_h$  is parallel with the orbit momentum vector and  $\hat{\mathbf{o}}_\theta$  completes the triad. A complete derivation of the relative equations of motion for eccentric orbits can be found in Ref. 13. If the relative orbit coordinates are small compared to the chief

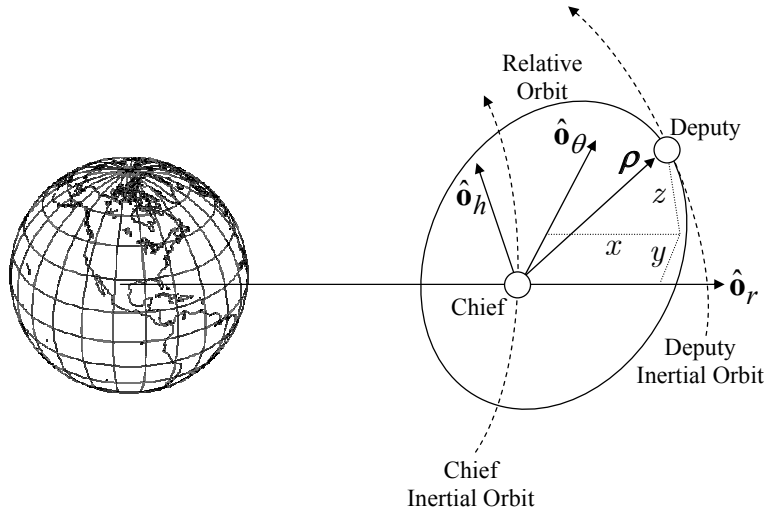


Figure 1. General Type of Spacecraft Formation with Relative Motion

orbit radius, then the equations of motion are given by (with disturbances added here)

$$\ddot{x} - x\dot{\theta}^2 \left(1 + 2\frac{r_c}{p}\right) - 2\dot{\theta} \left(\dot{y} - y\frac{\dot{r}_c}{r_c}\right) = w_1 \quad (1a)$$

$$\ddot{y} + 2\dot{\theta} \left(\dot{x} - x\frac{\dot{r}_c}{r_c}\right) - y\dot{\theta}^2 \left(1 - \frac{r_c}{p}\right) = w_2 \quad (1b)$$

$$\ddot{z} + z\dot{\theta}^2 \frac{r_c}{p} = w_3 \quad (1c)$$

where  $p$  is semilatus rectum of the chief,  $r_c$  is the chief orbit radius and  $\dot{\theta}$  is true anomaly rate of the chief. Also,  $w_1$ ,  $w_2$  and  $w_3$  are acceleration disturbances which are modeled as zero-mean Gaussian white-noise processes. The true anomaly acceleration and chief orbit-radius acceleration are given by

$$\ddot{\theta} = -2\frac{\dot{r}_c}{r_c}\dot{\theta} \quad (2a)$$

$$\ddot{r}_c = r_c\dot{\theta}^2 \left(1 - \frac{r_c}{p}\right) \quad (2b)$$

If the chief spacecraft orbit is assumed to be circular so that  $\dot{r}_c = 0$  and  $p = r_c$ , then the relative equations of motion reduce to the simple form known as the Clohessy-Wiltshire (CW) or Hill's equations:

$$\ddot{x} - 2n\dot{y} - 3n^2x = w_1 \quad (3a)$$

$$\ddot{y} + 2n\dot{x} = w_2 \quad (3b)$$

$$\ddot{z} + n^2z = w_3 \quad (3c)$$

where  $n = \dot{\theta}$  is the mean motion. The analyses in this paper are limited to the two-dimensional case but may be easily extended to three-dimensions, at the expense of significant additional computing time.

## A. Baseline Analysis

To begin a preliminary baseline analysis, a covariance analysis is performed. We begin with Hill's equations for in-plane (two-dimensional) motion only (the simplest form for relative motion of two spacecraft).<sup>13</sup> For convenience, Eq. (3) is repeated here without the out-of-plane  $z$  component:

$$\ddot{x} - 2n\dot{y} - 3n^2x = w_1 \quad (4a)$$

$$\ddot{y} + 2n\dot{x} = w_2 \quad (4b)$$

The state-space representation is given by

$$\dot{\mathbf{x}} = \begin{bmatrix} 0 & 0 & 1 & 0 \\ 0 & 0 & 0 & 1 \\ 3n^2 & 0 & 0 & 2n \\ 0 & 0 & -2n & 0 \end{bmatrix} \mathbf{x} + \begin{bmatrix} 0 & 0 \\ 0 & 0 \\ 1 & 0 \\ 0 & 1 \end{bmatrix} \mathbf{w} \quad (5a)$$

$$\equiv F \mathbf{x} + G \mathbf{w} \quad (5b)$$

where  $\mathbf{x} \equiv [x \ y \ \dot{x} \ \dot{y}]^T$  and  $\mathbf{w} \equiv [w_1 \ w_2]^T$  with covariance given by  $Q$ . The conversion of the system in Eq. (5) to discrete-time is given by van Loan<sup>14</sup> for fixed parameter systems, which includes a constant sampling interval and time-invariant state and covariance matrices.

First, the following augmented matrix is formed:

$$\mathcal{A} = \begin{bmatrix} -F & G Q G^T \\ 0 & F^T \end{bmatrix} \Delta t \quad (6)$$

where  $\Delta t$  is the constant sampling interval,  $F$  is the constant continuous-time state matrix, and  $Q$  is the constant continuous-time process noise covariance. Then, the matrix exponential of Eq. (6) is computed:

$$\mathcal{B} = e^{\mathcal{A}} \equiv \begin{bmatrix} \mathcal{B}_{11} & \mathcal{B}_{12} \\ 0 & \mathcal{B}_{22} \end{bmatrix} = \begin{bmatrix} \mathcal{B}_{11} & \Phi^{-1} Q \\ 0 & \Phi^T \end{bmatrix} \quad (7)$$

where  $\Phi$  is the state transition matrix of  $F$  and  $Q$  is the discrete-time process noise covariance matrix. The state transition matrix is then given by

$$\Phi = \mathcal{B}_{22}^T \quad (8)$$

Also, the discrete-time process noise covariance is given by

$$Q = \Phi \mathcal{B}_{12} \quad (9)$$

If the sampling interval is “small” enough, then obviously a first-order analysis is a good approximation for the solution given by Eqs. (8) and (9), with  $\Phi \approx I + \Delta t F$  and  $Q \approx \Delta t G Q G^T$ .

The output is assumed to be the LOS of one spacecraft to the other. Since we only have planar motion, then the LOS is simply given by one angle  $\theta$ :

$$\theta = \tan^{-1} \left( \frac{x}{y} \right) \quad (10)$$

The sensitivity matrix is formed by taking the partials of Eq. (10) with respect to  $x$  and  $y$ :

$$H = \begin{bmatrix} \frac{y}{x^2 + y^2} & \frac{-x}{x^2 + y^2} & 0 & 0 \end{bmatrix} \quad (11)$$

This is obviously nonlinear. To simplify the analysis it is assumed that  $x = y$  ( $\theta = 45^\circ$ ) and that the spacecraft are kept  $c$  km apart for all time (note that in principle, while  $c$  could be any constant,  $c$  is chosen to be 1 km for simplicity). This leads to

$$H = \frac{\sqrt{2}}{2c} \begin{bmatrix} 1 & -1 & 0 & 0 \end{bmatrix} \quad (12)$$

Other constant angles can be tested as well if desired. For example if we choose  $\theta = 0^\circ$ , then we have

$$H = \frac{1}{c} \begin{bmatrix} 1 & 0 & 0 & 0 \end{bmatrix} \quad (13)$$

Note that Eq. (12) (and Eq. (13)) may not be completely realistic, but for a baseline analysis they should be adequate. The steady-state Riccati equation can now be solved to determine the expected performance of the estimation state using a Kalman filter:<sup>12</sup>

$$P = \Phi P \Phi^T - \Phi P H^T [H P H^T + R]^{-1} H P \Phi^T + Q \quad (14)$$

where  $P$  is the covariance matrix of the estimation error,  $R$  is the measurement covariance (scalar for our case), and  $\Phi$  and  $Q$  are discrete-time versions of  $F$  and  $Q$ , respectively. The standard deviation of the filtered LOS estimate is given by

$$\sigma_{\text{LOS}} = (H P H^T)^{1/2} \quad (15)$$

Equation (15) can now be used to compute the required sensor noise accuracy and sampling interval to achieve the desired filtered LOS estimate.

An even simpler analysis can be performed by just considering the system as an attitude problem. This can be useful to quantify the general trends of the previous analysis. Suppose that we have the following model:

$$\dot{\bar{\mathbf{x}}} = \begin{bmatrix} 0 & 1 \\ 0 & 0 \end{bmatrix} \bar{\mathbf{x}} + \begin{bmatrix} 0 \\ 1 \end{bmatrix} \bar{w} \equiv \bar{F} \bar{\mathbf{x}} + \bar{G} \bar{w} \quad (16)$$

where  $\bar{\mathbf{x}} \equiv [\theta \ \omega]^T$ , with  $\omega = \dot{\theta}$  denoting ‘‘angular velocity,’’ and the variance of  $\bar{w}$  is given by  $\bar{q}$ . Now we assume continuous measurements with measurement noise  $R_{\text{cont}} = \sigma_{\text{sensor}}^2 \Delta t$  (see Ref. [15] for details), where  $\sigma_{\text{sensor}}^2$  is the standard deviation of the LOS measurement noise. This will be a reasonable approximation if the sampling interval is much shorter than the time constants of interest, which is the case of most interest. The covariance obeys

$$\dot{\bar{P}} = \bar{F} \bar{P} + \bar{P} \bar{F}^T - \bar{P} \bar{H}^T R_{\text{cont}}^{-1} \bar{H} \bar{P} + \bar{q} \bar{G} \bar{G}^T \quad (17)$$

with  $\bar{H} = [1 \ 0]$  and

$$\bar{P} \equiv \begin{bmatrix} \bar{P}_{\theta\theta} & \bar{P}_{\theta\omega} \\ \bar{P}_{\theta\omega} & \bar{P}_{\omega\omega} \end{bmatrix} \quad (18)$$

At steady state,  $\dot{\bar{P}} = 0$ , so

$$\begin{bmatrix} 2\bar{P}_{\theta\theta} & \bar{P}_{\omega\omega} \\ \bar{P}_{\omega\omega} & \bar{q} \end{bmatrix} - \frac{1}{\sigma_{\text{sensor}}^2 \Delta t} \begin{bmatrix} \bar{P}_{\theta\theta} \\ \bar{P}_{\theta\omega} \end{bmatrix} \begin{bmatrix} \bar{P}_{\theta\theta} & \bar{P}_{\theta\omega} \end{bmatrix} = 0 \quad (19)$$

Equation (19) can easily be solved to give

$$\bar{P}_{\theta\theta} = [4\bar{q}(\sigma_{\text{sensor}}^2 \Delta t)^3]^{1/4} \equiv \bar{\sigma}_{\text{LOS}}^2 \quad (20a)$$

$$\bar{P}_{\theta\omega} = (\bar{q} \sigma_{\text{sensor}}^2 \Delta t)^{1/2} \quad (20b)$$

$$\bar{P}_{\omega\omega} = (4\bar{q}^3 \sigma_{\text{sensor}}^2 \Delta t)^{1/4} \quad (20c)$$

Note that  $\bar{P}_{\theta\omega} = (\bar{P}_{\theta\theta} \bar{P}_{\omega\omega} / 2)^{1/2}$ . The LOS error is now given by

$$\bar{\sigma}_{\text{LOS}} = (4\bar{q})^{1/8} \sigma_{\text{sensor}}^{3/4} \Delta t^{3/8} \quad (21)$$

Equation (21) can be compared with Eq. (15) to investigate the general trends of the expected results for various levels of sensor accuracies and sampling intervals. Note that  $\bar{q}$  is not related to the  $Q$  in a direct manner, but the powers of  $\sigma_{\text{sensor}}$  and  $\Delta t$  in Eq. (21) do show relationships with the results obtained using Eq. (15).

## B. Expanded Analysis

To solve the Riccati equation, Eq. (14), in the simple baseline analysis above,  $P$  must be constant for a given  $\Delta t$ . In turn, this requires a constant  $H$  matrix (see Eq. (12) above) as well as constant  $\Phi$ ,  $R$ , and  $Q$ . As an aside, note from Eq. (15) that  $P$  is not used directly to determine the standard deviation of the filtered LOS estimate. The  $H P H^T$  term in Eq. (15) effectively gives the variance of the system in the direction of  $H$ .

An extended Kalman filter is necessary if the measurement model is nonlinear and changes with time (i.e. a time-varying  $H$  matrix). Several simulations are performed using different types of Kalman filters: a square-root Information Filter (SRIF), a square-root Unscented Kalman filter (SRUKF), and a square-root Kalman Filter (SRKF). Square-root filters are used primarily to improve precision and eliminate or reduce errors due to rounding or poorly conditioned matrices. Results from each Kalman filter are compared with the baseline analysis.

The SRIF uses the inverse of covariance matrix:<sup>16</sup>

$$\mathcal{P}_k^+ \equiv (P_k^+)^{-1} = \mathcal{S}_k^{+T} \mathcal{S}_k^+ \quad (22a)$$

$$\mathcal{P}_k^- \equiv (P_k^-)^{-1} = \mathcal{S}_k^{-T} \mathcal{S}_k^- \quad (22b)$$

where  $\mathcal{S} \equiv S^{-1}$ , and  $P_k^+$  and  $P_k^-$  are the updated and propagated covariances, respectively. A square root decomposition of the inverse measurement covariance and an eigenvalue decomposition of the process noise covariance is also used in the SRIF:

$$R_k^{-1} = \mathcal{V}_k^T \mathcal{V}_k \quad (23a)$$

$$\mathcal{Q}_k = Z_k E_k Z_k^T \quad (23b)$$

where  $\mathcal{V}_k$  is the inverse of the matrix  $V_k$  in  $R = V_k V_k^T$ . The matrix  $E_k$  is an  $s \times s$  diagonal matrix of the  $s$  non-zero eigenvalues of  $\mathcal{Q}_k$ . The matrix  $Z_k$  consists of eigenvectors of the corresponding non-zero eigenvalues. Next, the following  $(n+m) \times n$  matrix is formed, where  $n$  is the dimension of the state and  $m$  is the dimension of the output:

$$\tilde{\mathcal{S}}_k^+ \equiv \begin{bmatrix} \mathcal{S}_k^- \\ \mathcal{V}_k H_k \end{bmatrix} \quad (24)$$

It can be shown that when a  $QR$  decomposition of  $\tilde{\mathcal{S}}_k^+$  is taken, then the updated matrix  $\mathcal{S}_k^+$  can be extracted from

$$\mathcal{T}_k^T \tilde{\mathcal{S}}_k^+ = \begin{bmatrix} \mathcal{S}_k^+ \\ 0_{m \times n} \end{bmatrix} \quad (25)$$

where  $\mathcal{T}_k$  is the orthogonal matrix from the  $QR$  decomposition of  $\tilde{\mathcal{S}}_k^+$ . In the SRIF the state is not explicitly estimated. Instead the following quantities are used:

$$\hat{\alpha}_k^+ \equiv \mathcal{S}_k^+ \hat{\mathbf{x}}_k^+ \quad (26a)$$

$$\hat{\alpha}_k^- \equiv \mathcal{S}_k^- \hat{\mathbf{x}}_k^- \quad (26b)$$

Note the updated and propagated state can easily be found by taking the inverse of Eq. (26). The update equation is given by

$$\begin{bmatrix} \hat{\alpha}_k^+ \\ \beta_k \end{bmatrix} = \mathcal{T}_k^T \begin{bmatrix} \hat{\alpha}_k^- \\ \tilde{\mathbf{y}}_k \end{bmatrix} \quad (27)$$

where  $\beta_k$  is an  $m \times 1$  vector, which is the residual after processing the measurement, that is not required in the SRIF calculations. The following  $n \times s$  matrix is now defined:

$$\Xi_k \equiv \Upsilon_k Z_k \quad (28)$$

where  $\Upsilon_k$  is defined in the filter model (see Tables 1 and 2). Let  $\Xi_k(i)$  denote the  $i^{\text{th}}$  column of  $\Xi_k$  and  $E_k(i, i)$  denote the  $i^{\text{th}}$  diagonal value of the matrix  $E_k$ . The propagated values are given by a set of  $s$  iterations:

for  $i = 1$

$$\mathbf{a} = \mathcal{S}_k^+ \Phi_k^{-1} \Xi_k(1) \quad (29a)$$

$$\mathbf{b} = [\mathbf{a}^T \mathbf{a} + 1/E_k(1, 1)]^{-1} \quad (29b)$$

$$\mathbf{c} = [1 + \sqrt{\mathbf{b}/E_k(1, 1)}]^{-1} \quad (29c)$$

$$\mathbf{d}^T = \mathbf{b} \mathbf{a}^T \mathcal{S}_k^+ \Phi_k^{-1} \quad (29d)$$

$$\hat{\alpha}_{k+1}^- = \hat{\alpha}_k^+ - \mathbf{b} \mathbf{c} \mathbf{a} \mathbf{a}^T \hat{\alpha}_k^+ \quad (29e)$$

$$\mathcal{S}_{k+1}^- = \mathcal{S}_k^+ \Phi_k^{-1} - \mathbf{c} \mathbf{a} \mathbf{d}^T \quad (29f)$$

for  $i > 1$

$$\mathbf{a} = \mathcal{S}_{k+1}^- \Xi_k(i) \quad (30a)$$

$$b = [\mathbf{a}^T \mathbf{a} + 1/E_k(i, i)]^{-1} \quad (30b)$$

$$c = \left[1 + \sqrt{b/E_k(i, i)}\right]^{-1} \quad (30c)$$

$$\mathbf{d}^T = b \mathbf{a}^T \mathcal{S}_{k+1}^- \quad (30d)$$

$$\hat{\boldsymbol{\alpha}}_{k+1}^- \leftarrow \hat{\boldsymbol{\alpha}}_{k+1}^- - b c \mathbf{a} \mathbf{a}^T \hat{\boldsymbol{\alpha}}_{k+1}^- \quad (30e)$$

$$\mathcal{S}_{k+1}^- \leftarrow \mathcal{S}_{k+1}^- - c \mathbf{a} \mathbf{d}^T \quad (30f)$$

where  $\leftarrow$  denotes replacement. This SRIF is essentially a simplified version of the SRIF used. The main focus of this paper is to provide expected performance specifications. Therefore, state estimates are not explicitly required; only the covariance information is needed. Unfortunately, the LOS measurement equation is nonlinear in the state. However, a sufficient approach to overcome this difficulty is to use the true states in place of the estimated ones.<sup>15</sup> This significantly reduces the computational load, which can be significant for very small sampling intervals.

General algorithms for the SRUKF and SRKF are shown in Tables 1 and 2, respectively. In each table,  $\mathcal{Q}$  is the process noise covariance matrix and  $R$  is the measurement noise covariance matrix, while  $P_0$  is the initial covariance.

For the SRUKF in Table 1,  $n$  is the dimension of the state vector, while  $\gamma$  and  $W$  are standard Unscented filter parameters, defined by  $n$  and the choice of the parameters  $\alpha$ ,  $\beta$ , and  $\kappa$ . In the particular simulations run for this paper,  $n = 4$  and the remaining parameters are chosen as follows:  $\alpha = 1$ ,  $\beta = 2$ , and  $\kappa = 0$ . Note that the `cholupdate` function (available in MATLAB) is different from the `chol` function. The `cholupdate` function allows  $S$  to be updated, even if  $W_0^c$  is negative (in which case  $S$  would be “downdated”). See Refs. 17 and 18 for more details regarding the implementation and operation of the SRUKF.

The SRKF algorithm shown in Table 2 was derived after it was realized that if the process and measurement models are linear (as in this case) and we are not interested in updating the state vector (ultimately, we are only interested in the state covariance,  $P$  as this is essentially a covariance analysis) then it is not necessary to generate sigma points and the SRUKF essentially reduces to this form. Furthermore, since  $\Delta t$  and the errors are assumed to be very small, truth values can be used to update the sensitivity matrix,  $H$ , which is the same approach used in the SRIF.

### III. Results

In this section expected filtered LOS results are shown using some realistic parameters for the spacecraft disturbance effects. For both the baseline analysis and the expanded analysis, the principal simulation parameters are the same: The process noise covariance matrix  $Q$  is assumed to be given by a scalar times the identity matrix (i.e., isotropic errors) with  $Q = qI_{2 \times 2} \delta(t - \tau)$ , where  $\delta(t - \tau)$  is the Dirac delta function. A reasonable  $3\sigma$  outlier for the disturbances acting on the spacecraft is about a few micro g’s. Hence,  $q$  is given by  $(2 \times 9.81 \times 10^{-9}/3)^2 \text{ km}^2/\text{s}^4$ . The spacecraft are placed in low-Earth orbit ( $n = 0.0011 \text{ rad/sec}$ ) and they are assumed to be 1 km apart (i.e.  $c = 1$ ). This separation, of course, is true only at initial time for the expanded analyses.

Note that these analyses were run using MATLAB versions 6.5 (R13) and 7.2 (R2006a). The baseline analysis was run exclusively in MATLAB 7.2 to take advantage of the increased precision and numerical stability available in the `dare` function (due to square-root-based SLICOT routines introduced in Control System Toolbox v6.0/R14).<sup>19</sup>

#### A. Baseline Analysis

The sensitivity matrix for the baseline analysis is given by Eq. (12) with  $c = 1 \text{ km}$ . Using these parameters the steady-state covariance  $P$  is solved using Eq. (14), and the standard deviation of the expected filtered LOS estimate is computed using Eq. (15).

A 3D plot of the expected filtered LOS performance, derived using the steady-state Riccati solution in Eqs. (14) and (15), versus the sampling interval and sensor standard deviation is shown in Figure 2. From

Table 1. Square-Root Unscented Kalman Filter

Model	$\mathbf{x}_{k+1} = \mathbf{f}(\mathbf{x}_k, k) + \Upsilon_k \mathbf{w}_k$ $\tilde{\mathbf{y}}_k = \mathbf{h}(\mathbf{x}_k, k) + \mathbf{v}_k$
Initialize	$\hat{\mathbf{x}}(t_0) = \hat{\mathbf{x}}_0$ $S_0^+ = \text{chol}\{P_0\}$
Propagation	$\boldsymbol{\chi}_k(0) = \hat{\mathbf{x}}_k^+$ $\boldsymbol{\chi}_k(1 : 2n) = \begin{bmatrix} \hat{\mathbf{x}}_k^+ + \gamma S_k^+ & \hat{\mathbf{x}}_k^+ - \gamma S_k^+ \end{bmatrix}$ $\boldsymbol{\chi}_{k+1}(i) = \mathbf{f}[\boldsymbol{\chi}_k(i), k]$ $\hat{\mathbf{x}}_{k+1}^- = W_0^m \boldsymbol{\chi}_{k+1}(0) + \sum_{i=1}^{2n} W_i^m \boldsymbol{\chi}_{k+1}(i)$ $S_{k+1}^- = \text{qr} \left\{ \begin{bmatrix} \sqrt{W_1^c} (\boldsymbol{\chi}_{k+1}(1 : 2n) - \hat{\mathbf{x}}_{k+1}^-) & \Upsilon_k \sqrt{Q_k} \end{bmatrix} \right\}$ $S_{k+1}^- = \text{cholupdate} \{S_{k+1}^-, \boldsymbol{\chi}_{k+1}(0) - \hat{\mathbf{x}}_{k+1}^-, W_0^c\}$ $\boldsymbol{\chi}_{k+1}(0) = \hat{\mathbf{x}}_{k+1}^-$ $\boldsymbol{\chi}_{k+1}(1 : 2n) = \begin{bmatrix} \hat{\mathbf{x}}_{k+1}^- + \gamma S_{k+1}^- & \hat{\mathbf{x}}_{k+1}^- - \gamma S_{k+1}^- \end{bmatrix}$ $\boldsymbol{\mathcal{Y}}_{k+1}(i) = \mathbf{h}[\boldsymbol{\chi}_{k+1}(i), k]$ $\hat{\mathbf{y}}_{k+1}^- = W_0^m \boldsymbol{\mathcal{Y}}_{k+1}(0) + \sum_{i=1}^{2n} W_i^m \boldsymbol{\mathcal{Y}}_{k+1}(i)$ $S_{k+1}^y = \text{qr} \left\{ \begin{bmatrix} \sqrt{W_1^c} (\boldsymbol{\mathcal{Y}}_{k+1}(1 : 2n) - \hat{\mathbf{y}}_{k+1}^-) & \sqrt{R_{k+1}} \end{bmatrix} \right\}$ $S_{k+1}^y = \text{cholupdate} \{S_{k+1}^y, \boldsymbol{\mathcal{Y}}_{k+1}(0) - \hat{\mathbf{y}}_{k+1}^-, W_0^c\}$ $P_{k+1}^{xy} = \sum_{i=0}^{2n} W_i^c [\boldsymbol{\chi}_{k+1}(i) - \hat{\mathbf{x}}_{k+1}^-] [\boldsymbol{\mathcal{Y}}_{k+1}(i) - \hat{\mathbf{y}}_{k+1}^-]^T$
Gain	$K_{k+1} = (P_{k+1}^{xy} / S_{k+1}^{yT}) / S_{k+1}^y$
Update	$\mathbf{v}_{k+1} \equiv \tilde{\mathbf{y}}_{k+1} - \hat{\mathbf{y}}_{k+1}^-$ $\hat{\mathbf{x}}_{k+1}^+ = \hat{\mathbf{x}}_{k+1}^- + K_{k+1} \mathbf{v}_{k+1}$ $S_{k+1}^+ = \text{cholupdate} \{S_{k+1}^-, K_{k+1} S_{k+1}^y, -1\}$

this analysis, achieving near micro-arcsec performance is possible with a sampling interval of  $1 \times 10^{-6}$  seconds and sensor standard deviation of  $1 \times 10^{-4}$  arcsec. Note that the 3D surface does not form a plane. To further see this behavior, various slices of this surface are shown in the plots of Figure 3. Figure 3(a) shows a linear relationship with respect to varying sampling interval and a sensor standard deviation of 1 arcsec. The slope of this curve is nearly 3/8, which matches well with the simplified relationship shown in Eq. (21). For a smaller sensor standard deviation ( $1 \times 10^{-4}$  arcsec), a nonlinear relationship exists with respect to sampling interval, as shown in Figure 3(b). However, the slope for small sampling intervals is nearly 3/8, which again matches well with the simplified relationship. Figures 3(c) and Figure 3(d) show results for sampling intervals of 1 second and  $1 \times 10^{-6}$  seconds, respectively, with varying sensor noise standard deviation. The slope of the linear region in Figure 3(c) is given by 3/4, which matches well with the simplified relationship

**Table 2. Square-Root Kalman Filter**

Model	$\mathbf{x}_{k+1} = \Phi_k \mathbf{x}_k + \Upsilon_k \mathbf{w}_k$ $\tilde{\mathbf{y}}_k = H_k \mathbf{x}_k + \mathbf{v}_k$
Initialize	$\hat{\mathbf{x}}(t_0) = \hat{\mathbf{x}}_0$ $S_0^+ = \text{chol}\{P_0\}$
Propagation	$\hat{\mathbf{x}}_{k+1}^- = \Phi_k \hat{\mathbf{x}}_k^+$ $\hat{\mathbf{y}}_{k+1}^- = H_{k+1} \hat{\mathbf{x}}_{k+1}^-$ $S_{k+1}^- = \text{qr}\left\{\begin{bmatrix} \Phi_k S_k^+ & \Upsilon_k \sqrt{Q_k} \end{bmatrix}\right\}$ $S_{k+1}^y = \text{qr}\left\{\begin{bmatrix} H_{k+1} S_{k+1}^- & \sqrt{R_{k+1}} \end{bmatrix}\right\}$ $P_{k+1}^{xy} = S_{k+1}^- S_{k+1}^{-T} H_{k+1}^T$
Gain	$K_{k+1} = (P_{k+1}^{xy} / S_{k+1}^{yT}) / S_{k+1}^y$
Update	$\mathbf{v}_{k+1} \equiv \tilde{\mathbf{y}}_{k+1} - \hat{\mathbf{y}}_{k+1}^-$ $\hat{\mathbf{x}}_{k+1}^+ = \hat{\mathbf{x}}_{k+1}^- + K_{k+1} \mathbf{v}_{k+1}$ $S_{k+1}^+ = \text{cholupdate}\{S_{k+1}^-, K_{k+1} S_{k+1}^y, -1\}$

shown in Eq. (21). The slope shown in Figure 3(d) is 3/4 as well. These plots indicate that the slopes are not linear when the sampling interval is large and the sensor noise is small. But, the simplified relationship of Eq. (21) shows excellent agreement with the Riccati solution in the linear regions.

Better than micro-arcsec performance is shown in Figure 4 with a sampling interval of  $1 \times 10^{-5}$  seconds and sensor standard deviation of  $1 \times 10^{-5}$  arcsec. Note the “spikes” in Figure 4, which are an indication of some of the numerical problems inherent to solving the algebraic Riccati equation. This and other numerical issues are motivation to verify and expand this analysis through the use of different types of square-root Kalman filters.

## B. Expanded Analysis

The results in Figures 5 and 6 are obtained using the SRUKF. These results are very close to the results in Figures 2, 3 and 4 using the Riccati solutions for LOS accuracy. The LOS variances are calculated using the sigma points and unscented transformation. They agree well with Eq. (15) because  $P$  is very small. Note that the LOS Accuracy in Figures 5 and 6 are actual values and are not plotted on a log scale.

The initial condition of the state is  $\mathbf{x}(t_0) = [0 \ 1 \ 0.5n \ 0]^T$  with  $n = 0.0011$ . Under the noise-free assumption, the nominal motion of the first two state variables is given by  $[0.5 \sin(nt) \ \cos(nt)]^T$ . The relative position of the deputy is not entirely observable because the only measurement available to the system is the angle  $\theta$  in the LOS direction—there is no range measurement. In other words, the filter can easily predict and correct the course *along track* but there is virtually no information available regarding movement in the radial direction (though there is a very small amount of coupling in the system due to the orbit dynamics). Thus,  $P$  will likely become more poorly conditioned as the sampling interval decreases. Evidence for this is shown in Figure 6 with increasing variance over time. These results are very similar to the results of the square-root information filter (SRIF) and the square-root Kalman filter (SRKF) with the same time-varying measurement model and, thus, the SRIF and SRKF results are not shown.

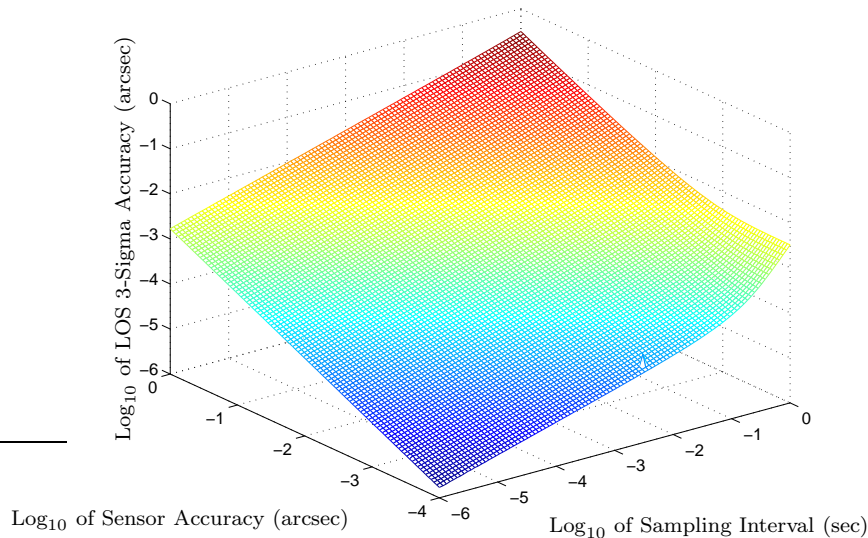


**Figure 2. Expected Performance Versus Sampling Interval and Sensor Accuracy**

## IV. Conclusion

This paper presented an analysis of the filtered performance from line-of-sight measurements for formation flying applications. The dynamics model was based on Hill's equations, which describe the relative motion between two spacecraft. Two variables were used for the expected filter performance analysis: sensor accuracy and sampling interval. A linear model was used to assess the expected performance from a steady-state Riccati solution, followed by a simplified analytical analysis that relates sensor accuracy and sampling interval to filtered performance. Filter solutions using the nonlinear output equation were also implemented, based on using various square-root Kalman filters and the square-root Unscented Kalman filter. These filters were chosen in order to reduce numerical problems. The linear model and simplified analysis showed good agreement with the filter solutions, thus reinforcing analytical predictions. The main goal is to assess the hardware requirements to achieve micro-arcsec performance. One possible combination for achieving this performance level uses a sampling interval of  $1 \times 10^{-6}$  seconds and sensor standard deviation of  $1 \times 10^{-4}$  arcsec. Another combination uses a sampling interval of  $1 \times 10^{-5}$  seconds and sensor standard deviation of  $1 \times 10^{-5}$  arcsec. Note that micro-g control will almost certainly be possible in the near future, and may already be possible given the capabilities of missions like Gravity Probe B. In addition, interferometry missions and the like will depend only upon the ability to control the relative positions of spacecraft with respect to disturbances (not the absolute positions of individual spacecraft), which will minimize these effects because all spacecraft will generally be subject to the same disturbances. Although technology currently does not exist to achieve micro-arcsec performance, the analysis shown in this paper shows system trades between sampling interval and sensor accuracy to achieve this performance level.

## V. Acknowledgments

The authors would like to thank F. Landis Markley from NASA Goddard Space Flight Center, and Kok-Lam Lai and Yang Cheng, from the University of Buffalo, State University of New York, without whom this paper would not be possible. The first author's work is sponsored through the NASA Graduate Student Research Program (GSRP). This support is greatly appreciated.

## References

<sup>1</sup>Aldridge, E. C., e. a., "A Journey to Inspire, Innovate, and Discover, Report of the President's Commission on Implementation of United States Space Exploration Policy," June 2004, [http://www.nasa.gov/pdf/60736main\\_M2M\\_report\\_small.pdf](http://www.nasa.gov/pdf/60736main_M2M_report_small.pdf).

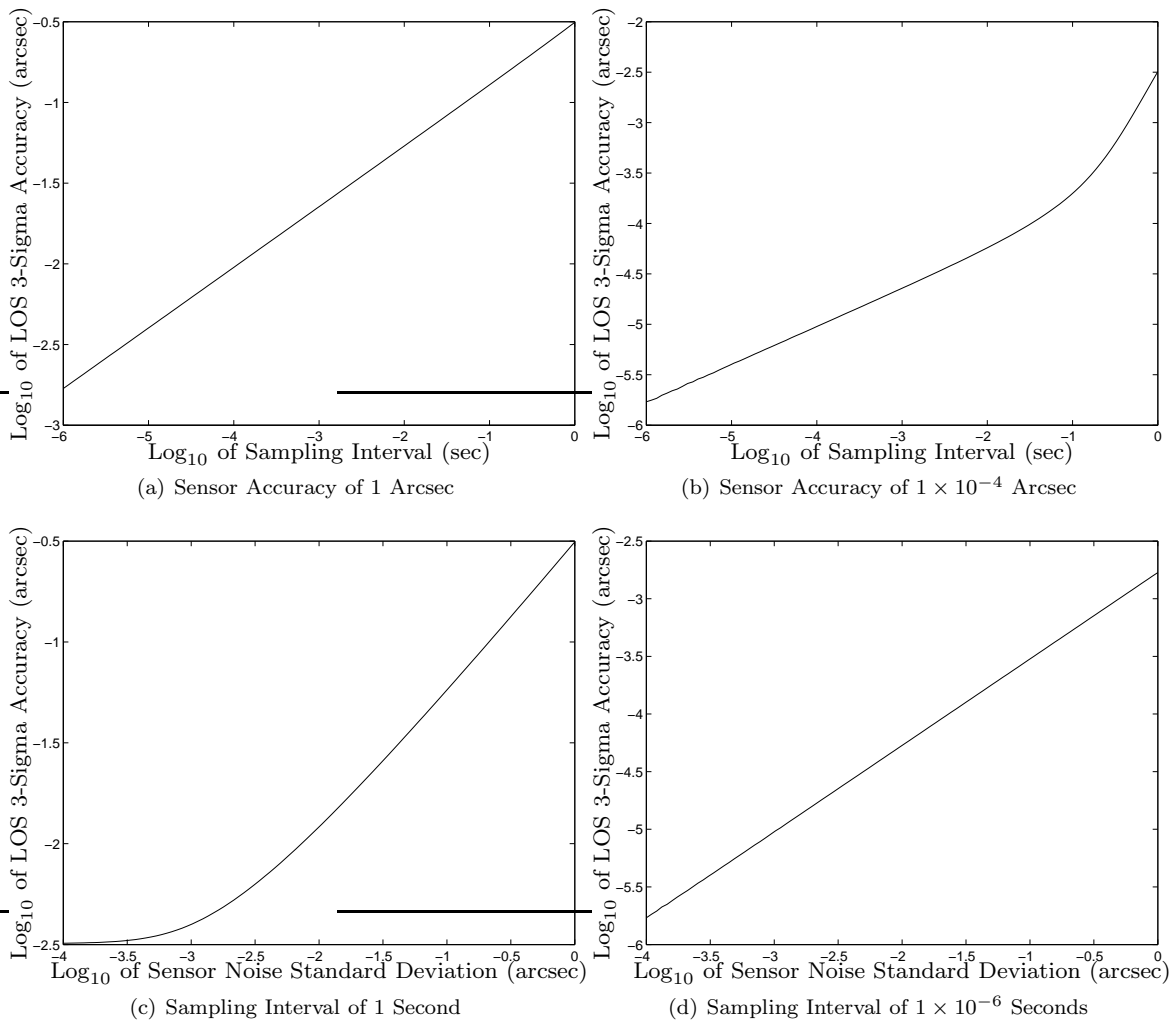


**Figure 3. Expected Performance Versus Various Sampling Intervals and Sensor Accuracies for Riccati Analysis**

<sup>2</sup>Carpenter, J., Leitner, J., Folta, D., and Burns, R., "Benchmark Problems for Spacecraft Formation Flying Missions," *AIAA Guidance, Navigation, and Control Conference*, Austin, TX, Aug. 2003, AIAA-2003-5364.

<sup>3</sup>Leitner, J., e. a., "Formation Flight in Space: Distributed Spacecraft Systems Develop New GPS Capabilities," *GPS World*, Feb. 2001.

<sup>4</sup>NASA Goddard Space Flight Center, *Constellation-X Mission*, <http://constellation.gsfc.nasa.gov/public/mission/index.html>, accessed 20 January 2006.

<sup>5</sup>Gendreau, K. C., e. a., "Requirements and Options for a Stable Inertial Reference Frame for a 100 micro-arcsecond Imaging Telescope," *SPIE Conference on Visualization and Data Analysis*, San Jose, CA, 20-25 Jan. 2002.

<sup>6</sup>NASA Goddard Space Flight Center, *DSS Mission List*, <http://gsfctechnology.gsfc.nasa.gov/dssmissionlist.htm>, accessed 14 January 2005.

<sup>7</sup>NASA Jet Propulsion Laboratory, *Space Technology 3 Mission*, <http://nmp.jpl.nasa.gov/st3/proj/>, accessed 20 January 2006.

<sup>8</sup>NASA Goddard Space Flight Center, *Stellar Imager Mission*, <http://hires.gsfc.nasa.gov/si/>, accessed 20 January 2006.

<sup>9</sup>NASA Goddard Space Flight Center, *MAXIM Mission*, <http://maxim.gsfc.nasa.gov/docs/mission/mission.html>, accessed 20 January 2006.

<sup>10</sup>Gunnam, K. K., Hughes, D. C., Junkins, J. L., and Kehtarnavaz, N., "A Vision-Based DSP Embedded Navigation Sensor," *IEEE Sensors Journal*, Vol. 2, No. 5, Oct. 2002, pp. 428-442.

<sup>11</sup>Kim, S.-G., Crassidis, J. L., Cheng, Y., Fosbury, A. M., and Junkins, J. L., "Kalman Filtering for Relative Spacecraft Attitude and Position Estimation," *AIAA Guidance, Navigation, and Control Conference*, San Francisco, CA, Aug. 2005, AIAA-05-6087.

<sup>12</sup>Crassidis, J. L. and Junkins, J. L., *Optimal Estimation of Dynamic Systems*, chap. 7, Chapman & Hall/CRC, Boca Raton, FL, 2004.

<sup>13</sup>Schaub, H. and Junkins, J. L., *Analytical Mechanics of Aerospace Systems*, chap. 14, American Institute of Aeronautics and Astronautics, Inc., New York, NY, 2003.

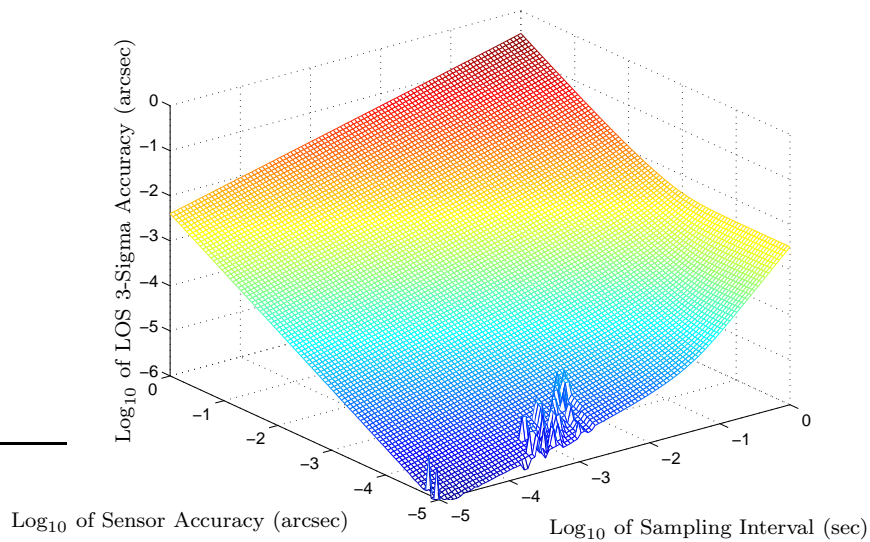


**Figure 4. Expected Performance Versus Sampling Interval and Sensor Accuracy for Riccati Analysis (Micro-arcsec Performance)**

<sup>14</sup>van Loan, C. F., "Computing Integrals Involving the Matrix Exponential," *IEEE Transactions on Automatic Control*, Vol. AC-23, No. 3, June 1978, pp. 396–404.

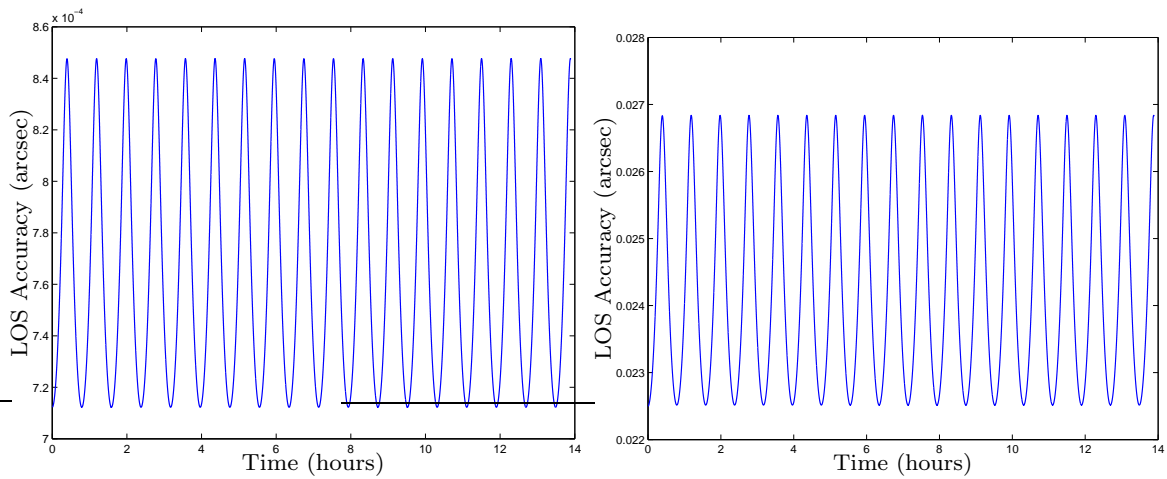
<sup>15</sup>Gelb, A., editor, *Applied Optimal Estimation*, The MIT Press, Cambridge, MA, 1974, pp. 135–136.

<sup>16</sup>Maybeck, P. S., *Stochastic Models, Estimation, and Control*, Vol. 1, Academic Press, New York, NY, 1979.

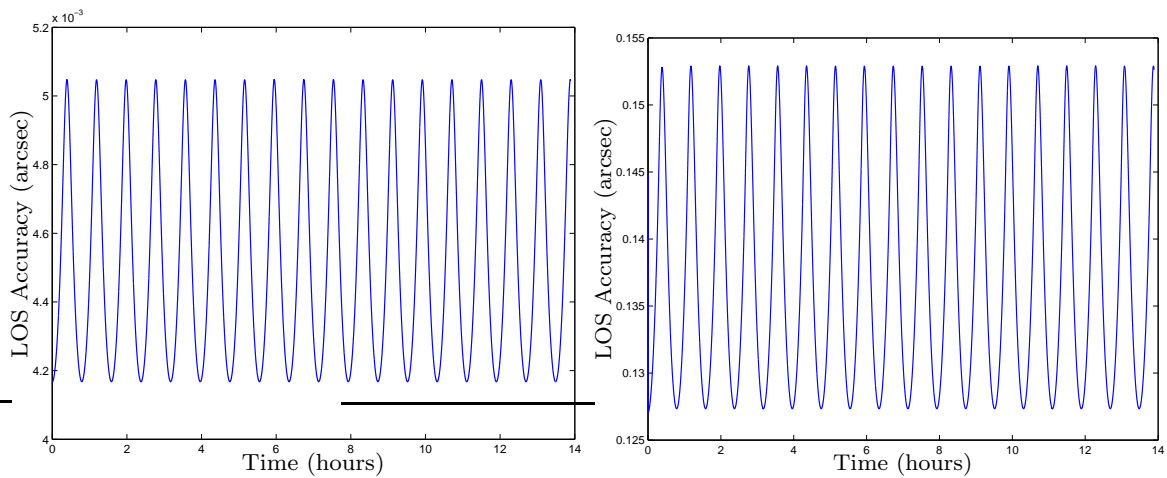
<sup>17</sup>van der Merwe, R. and Wan, E. A., "Square-Root Unscented Kalman Filter for State and Parameter-Estimation," *Proceedings of the IEEE International Conference on Acoustics, Speech, and Signal Processing*, Salt Lake City, UT, May 2001, pp. 3461–3464.

<sup>18</sup>Wan, E. and van der Merwe, R., "The Unscented Kalman Filter," *Kalman Filtering and Neural Networks*, edited by S. Haykin, chap. 7, John Wiley & Sons, New York, NY, 2001.

<sup>19</sup>The MathWorks, Inc., *Control System Toolbox Release Notes*, <http://www.mathworks.com/access/helpdesk/help/pdfdoc/control/rn.pdf>, accessed 5 August 2006.

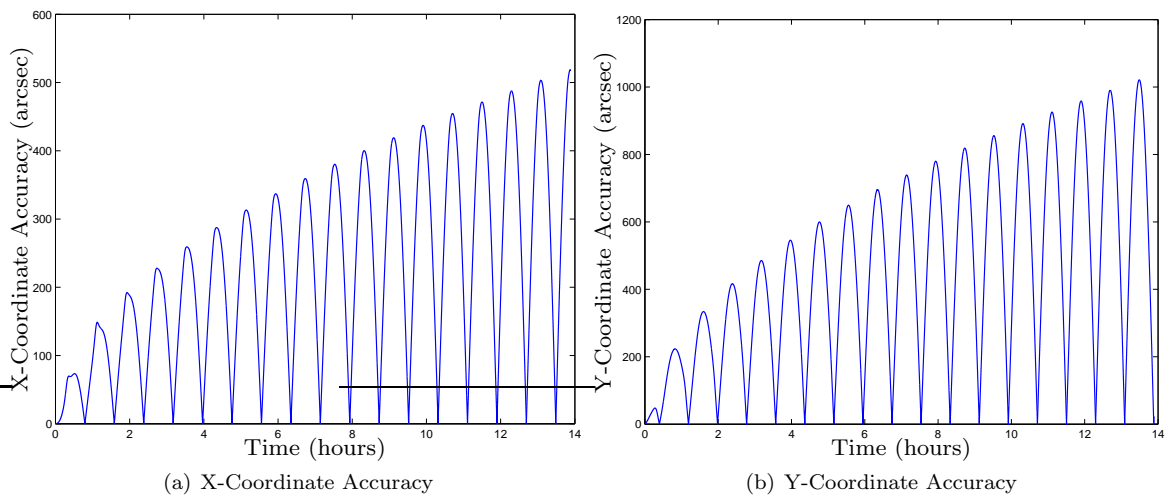


(a) Sampling Interval of 0.001 Seconds, Sensor Accuracy of 0.01 Arcsec (b) Sampling Interval of 0.001 Seconds, Sensor Accuracy of 1 Arcsec



(c) Sampling Interval of 0.1 Seconds, Sensor Accuracy of 0.01 Arcsec (d) Sampling Interval of 0.1 Seconds, Sensor Accuracy of 1 Arcsec

**Figure 5. Expected Performance Versus Various Sampling Intervals and Sensor Accuracies for SRUKF Analysis**



(a) X-Coordinate Accuracy (b) Y-Coordinate Accuracy

**Figure 6. X and Y Coordinate Accuracy for Sampling Interval of 0.1 Seconds and Sensor Accuracy of 1 Arcsec from SRUKF Analysis, Figure 5(d)**